INSERT CREATIVE NAME HERE

Author's name

Bachelorarbeit in Physik
angefertigt im Argelander-Institut für Astronomie

vorgelegt der
Mathematisch-Naturwissenschaftlichen Fakultät
der
Rheinischen Friedrich-Wilhelms-Universität
Bonn

MMM 2024

Ich versichere, dass ich diese Arbeit selbstständig verfasst und keine anderen als die angegebenen Quellen und Hilfsmittel benutzt sowie die Zitate kenntlich gemacht habe.

Bonn, ...

Datum Unterschrift

1. Gutachter: Prof. Dr. John Smith
2. Gutachterin: Prof. Dr. Anne Jones

Acknowledgements

I would like to thank ...

You should probably use `\chapter*` for acknowledgements at the beginning of a thesis and `\chapter` for the end.

Contents

CHAPTER 1

Introduction

Unlike the larger and more massive galaxy clusters, galaxy groups are smaller systems with typical masses around $3 \times 10^{13} M_{\odot}$ (Schneider, 2006). Despite their relative modest size, the study of galaxy groups is fundamental to our understanding of the Universe's large-scale structure (LSS), as they likely contain a significant fraction of the total baryonic mass in the Universe (Fukugita, Hogan, and Peebles, 1998). The space between galaxy clusters and groups is characterized by a hot, ionized gas known as the intracluster medium (ICM) or the intragroup medium (IGM), which fills the space between the galaxies. This gas emits copious amounts of X-rays making X-ray observations an essential tool for identifying and studying these structures (Kravtsov and Borgani, 2012).

The galaxy group NGC1550, first linked to the extended X-ray source RX J0419+0225 through the ROSAT All-Sky Survey (Böhringer et al., 2000), has been the subject of extensive X-ray observations. Analysis have been conducted using data from various instruments, including ASCA (Kawaharada, Makishima, Takahashi, et al., 2003), XMM-Newton (Kawaharada, Makishima, Kitaguchi, et al., 2009), Chandra (Sun et al., 2003), and Suzaku (Sato et al., 2010). In this thesis, data gathered with the *extended ROentgen Survey with an Imaging Telescope Array* (eROSITA) shall be utilized to characterize the X-ray surface brightness profile of NGC1550 and compare the results with previous studies.

Following a brief overview of the theoretical background in Chapter 2, Chapter 3 will focus on reducing and correcting the data for instrumental and background contamination sources. Chapter 4 will analyze the surface brightness profile of NGC1550, including a beta model fitting of the full azimuthal profile. Additionally, the analysis will compare the north, south, east, and west sectors against each other and against the full azimuthal profile. Chapter 5 will summarize all results, offer suggestions for improvement and for future works.

CHAPTER 2

Theoretical Background

2.1 Clusters and groups of galaxies

Throughout the Universe, galaxies are not distributed homogeneously but are instead aggregated into large cosmic structures known as galaxy groups or galaxy clusters, which are the largest relaxed structures in the Universe. Galaxy clusters typically have masses exceeding $M \gtrsim 3 \times 10^{14} M_{\odot}$, whereas galaxy groups have masses around $M \sim 3 \times 10^{13} M_{\odot}$ (Schneider, 2006). Advancements in X-ray astronomy have demonstrated that these structures are significant sources of X-ray radiation (A. G. Cavaliere, Gurksy, and Tucker, 1971). This emission is well understood to originate from a hot intergalactic gas known as the intracluster medium (ICM)[1], which is characterized by temperatures in the range of 10^7 to 10^8 K and constitutes the primary baryonic component of galaxy clusters and groups (Schneider, 2006).

2.1.1 The Intracluster Medium

Within the deep gravitational wells of galaxy clusters and groups, the temperature becomes sufficiently high to fully ionize lighter elements and partially ionize heavier elements, resulting in the formation of a plasma. This hot, diffuse, and optically thin plasma, known as the intracluster medium (ICM), emits a significant amount of X-ray radiation. X-ray observations of the ICM have enabled a wide variety of cosmological studies, including advances in understanding the large-scale structure formation in the Universe (Kravtsov and Borgani, 2012).

2.1.2 Emission Processes within the ICM

A key principle of electrodynamics is that accelerated charges radiate energy. This radiation is referred to as bremsstrahlung or "free-free" when a unbound charged particle, typically an electron, is accelerated by the electric field of other charges, usually ions. In the ICM, this process predominates at temperatures above $k_B T_{\rm e} \gtrsim 2\,\mathrm{keV}$, where the total emissivity $\epsilon_{\rm ff}$ at solar metallicity scales

[1] The intercluster medium is also called the intragroup medium (IGM) in the case of galaxy groups. In the context of this thesis, the terms ICM and IGM will be used interchangeably, as a distinction between them is not necessary.

approximately as $\epsilon_{\text{ff}} \propto T_{\text{e}}^{0.5} n_{\text{e}}$, with n_{e} and T_{e} as the electron number density and temperature, respectively. At lower temperatures ($k_B T \lesssim 2\,\text{keV}$), line emission becomes significant, with the emissivity being roughly described by $\epsilon \propto T_{\text{e}}^{-0.6} n_{\text{e}}$. Thus, for the low energy band 0.1 to 2.4 keV, one roughly finds that $\epsilon \propto n_{\text{e}}^2$. (Reiprich and Pacaud, 2019).

2.1.3 The beta model of the ICM

In the mid-1970s, A. Cavaliere and Fusco-Femiano, 1976 laid the groundwork for the current understanding of the ICM. The X-ray morphology of clusters and groups is typically described by the beta model. This model assumes gas and galaxies share the same gravitational potential. Given a constant temperature T and velocity dispersion σ_r, the radial distributions of the gas n_{gas} and galaxies ρ_{gal} obey

$$\frac{n_{\text{gas}}(r)}{n_{\text{gas}}(0)} = \left[\frac{\rho_{\text{gal}}(r)}{\rho_{\text{gal}(0)}}\right]^{\beta} ; \quad \beta = \frac{\mu m_p \sigma_r^2}{k_B T}$$

where μ is the mean molecular mass, m_p is the proton mass and k_B is the Boltzmann constant. Using the King approximation, which d $\rho_{\text{gal}}(r) = \rho_{\text{gal}}(0)\left[1 + (r/r_c)^2\right]^{-3/2}$ (King, 1962) where r_c is the core radius and $\epsilon \propto n_e^2$, the X-ray surface brightness S_X, obtained by integrating over the emissivity, follows the profile

$$S_X(r) = S_X(0)\left[1 + \left(\frac{r}{r_c}\right)^2\right]^{-3\beta+1/2} .$$

The beta model is widely used to describe cluster and group emissions, despite the assumptions listed above often being unmet. Excess core emission, for example, is typically addressed by adding a second beta model component: $S_X^{\text{tot}} = S_{X,1} + S_{X,2}$ (Reiprich and Pacaud, 2019).

2.1.4 The galaxy group NGC1550

The galaxy group NGC1550 is located at a right ascension of 64.9066° and a declination of 2.4151°, with a redshift of $z = 0.0123$ (Reiprich and Böhringer, 2002). Although the lenticular galaxy NGC 1550 has long been observable in the optical, it was first associated with the extended X-ray source RX J0419+0225 through the ROSAT All-Sky Survey (Böhringer et al., 2000). The presence of this extensive X-ray halo, along with its considerable mass ($\sim 2 \times 10^{13} M_\odot$), led to its classification as a galaxy group (Kawaharada, Makishima, Takahashi, et al., 2003).

Recent studies indicate that NGC1550 does not meet the formal criteria for a fossil group (Sun et al., 2003; cf. Jones et al., 2003 for the criteria), but it shares several features with such groups. One notable characteristic is its high X-ray bolometric luminosity ($\gtrsim 4.8 \times 10^{41}$ erg), which predominantly originates from a central, dominant, early-type galaxy. Fossil groups are thought to be formed when member galaxies in a regular galaxy group merge into a central dominant galaxy, and evidence for this process has been found in the metal distribution of NGC1550 (Kawaharada, Makishima, Kitaguchi, et al., 2009; Sato et al., 2010). Additionally, a recent study has identified signs of AGN (active galactic nucleus) feedback and sloshing, suggesting a minor merger occurred around 33 million years ago (Kolokythas et al., 2020). While the group appears to be relaxed overall, a slight east-west elongation in the central region has been noted by multiple authors (Kolokythas et al., 2020; Sun et al., 2003).

2.2 eROSITA

The *extended ROentgen Survey with an Imaging Telescope Array* (eROSITA) is a highly sensitive, wide-field X-ray telescope designed to capture deep images across large areas of the sky. Mounted on the Spektrum-Roentgen-Gamma (SRG) observatory in a halo orbit around the second Lagrange Point (L2), eROSITA operates within the 0.2 to 10.0 keV energy range. It is the first instrument to perform an all-sky imaging survey in the hard X-ray band (2.0 to 10.0 keV). In the soft X-ray band (0.5 to 2.0 keV), eROSITA boasts a sensitivity that is approximately 20 times greater than that of its predecessor, the ROSAT All-Sky Survey. eROSITA features seven identical mirror modules, known as Telescope Modules (TMs), with 54 mirror shells in Wolter-I geometry and a 1.6-meter focal length. Five TMs (TM1, TM2, TM3, TM4 and TM6) have aluminum on-chip optical light filters and are collectively referred to as TM8. The remaining two TMs (TM5, TM7), designed for low-energy spectroscopy, lack these filters and are referred to as TM9. Collectively, TM8 and TM9 are referred to as TM0. (Predehl et al., 2021). In this thesis, data from the first all-sky survey (eRASS:1) will be utilized. The data is provided in the form of event lists, which essentially detail the spatial position of X-ray photon arrivals on the detector, their time of arrival, and their energy. The event lists are made available in $3.6^\circ \times 3.6^\circ$ regions known as skytiles.

2.3 Sky background and contamination sources

For a thorough analysis of X-ray photons, it is essential to carefully consider both external background and internal instrumental contamination effects. The following section will provide a brief overview of the most important factors relevant to this analysis.

Cosmic X-ray Background (CXB): The cosmic X-ray background (CXB) comprises multiple sources, including diffuse, unabsorbed thermal emissions from the Local Hot Bubble, a plasma cavity surrounding the Sun, and absorbed thermal emissions from the Galactic halo (Galeazzi et al., 2006). Additionally, it includes discrete extragalactic sources, predominantly unresolved AGNs (Brandt and Hasinger, 2005). The diffuse component is more prominent in the lower energy band ~ 1 keV, while the extragalactic sources dominate at higher energies. In this analysis, background emission from the nearby Orion-Eridanus superbubble, which spans roughly 40° on the sky, shall also be present, as it emits in the soft X-ray regime (Krause et al., 2014). Figure 2.1, taken from Krause et al., 2014, shows an X-ray map of the Orion-Eridanus superbubble in the 0.5 to 2.0 keV band, illustrating its overlap with the galaxy group NGC1550.

Non-X-ray Background (NXB): The non-X-ray background consists of two main components: highly variable soft protons flares (SPF) from the solar corona and Earth's magnetosphere, which can

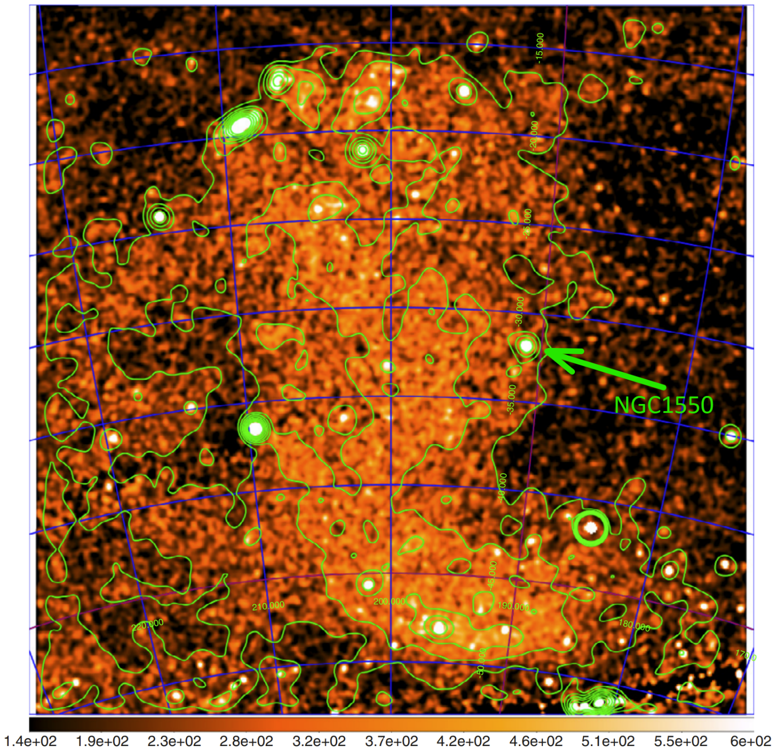

Figure 2.1: X-ray map in galactic coordinates of the Orion-Eridanus superbubble in the 0.5 to 2.0 keV band from the ROSAT all-sky survey. The colorbar units are 10^{-6} cts · arcmin^{-2}s^{-1} and the contour levels are 220, 300, 380, 460, 540, 620, 700. The image was taken from Krause et al., 2014. The green arrow and label were added to highlight the position of NGC1550.

be focused onto detectors, and energetic Galactic Cosmic Ray (GCR) primaries, which interact with the detector to produce secondary particles. While primary GCR events can mostly be discarded by onboard processing, the secondary particles deposit charge in the detector, making it challenging to distinguish them from true X-ray events. This is generally referred to as the particle-induced background (PIB) (Bulbul et al., 2020).

eROSITA light leak: Shortly after the launch of eROSITA, it was observed that CCDs lacking an on-chip filter (TM9) recorded a notably higher number of events. This was attributed to optical and ultraviolet light from the Sun entering the CCD through an unidentified gap in the detector shielding, and was subsequently termed “light-leak” (Predehl et al., 2021).

N_{H} absorption: As X-rays travel to the detector, they undergo photoelectric absorption in the interstellar and intergalactic medium. The cross-section $\sigma \propto E^{-3}$ is inversely proportional to energy, causing a bias toward harder X-rays, as they interact less. Additionally, the cross-section is proportional to the atomic number, $\sigma \propto Z^5$, making metal abundance crucial for energies $\gtrsim 0.2$ keV

(Willingale et al., 2013).

CHAPTER 3

Data Reduction

In the following section, the underlying data shall be reduced and corrected for the various effects and contamination sources explained in Section 2.3. Data from eRASS:1 and all TMs (1-7) are utilized using the *eROSITA* pipeline processing version c010. The galaxy group NGC1550 is located in skytile 065087. In addition, the surrounding skytiles 062084, 062087, 062090, 065084, 065090, 068084, 068087, and 068090 are used to encompass regions up to $\sim 3R_{200}$ (cf. value below). The data reduction is performed with the software HEASoft version[1] 6.29 and the extended Science Analysis Software System[2] (eSASS 4DR1).

Values for R_{200} and R_{500} were taken from Reiprich and Böhringer, 2002 and converted to $R_{200} = 58.58'$ and $R_{500} = 37.15'$ based on the cosmology used in this paper. The cosmology assumes $\Omega_m = 0.3, \Omega_\Lambda = 0.7$ and $h = 0.7$, where $1'' = 0.252\,\mathrm{kpc}$. For image creation, the Matplotlib (Hunter, 2007) and Astropy (Collaboration et al., 2022) Python-packages were utilized.

3.1 Raw photon images

Before the data reduction process, raw photon images for all combined skytiles and TMs are presented across the following energy bands: 0.2 to 2.3 keV, 2.3 to 6.0 keV, and 6.0 to 9.0 keV. The skytiles were combined using the *eSASS* task `evtool`, with no additional parameters applied to show all inherent deficiencies. The raw photon images are presented in Figure 3.1. A noticeable count drop on the right side of the images is evident and will be addressed through the exposure map correction detailed in Section 3.6. As observed, the group emission is mainly concentrated in the lower energy band, making the low energy band the focus for detecting emission structures. In this analysis, the 0.2 to 2.3 keV energy band is used. Due to the light-leak in TM9, however, the energy range is restricted to 0.8 to 2.3 keV, while it remains 0.2 to 2.3 keV for TM8. Hereafter, this TM-dependent energy band will be referred to as the "soft-band" and the 6.0 to 9.0 keV energy range as the "hard-band".

[1] https://heasarc.gsfc.nasa.gov/docs/software/heasoft/ (Last accessed: 04.08.2024)
[2] https://erosita.mpe.mpg.de/dr1/eSASS4DR1/ (Last accessed: 04.08.2024)

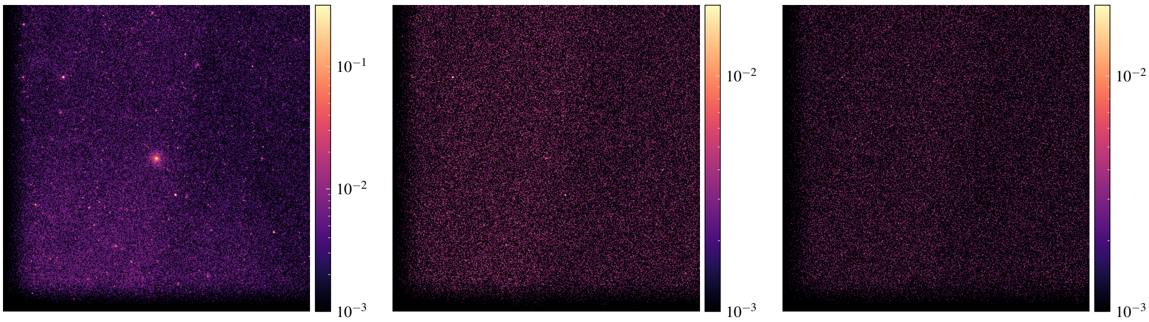

(a) 0.2 to 2.3 keV (b) 2.3 to 6.0 keV (c) 6.0 to 9.0 keV

Figure 3.1: Raw photon images from TM0 of all combined skytiles centered around NGC1550, displayed in the energy bands 0.2 to 2.3 keV (left), 2.3 to 6.0 keV (middle), and 6.0 to 9.0 keV (right), with Gaussian smoothing of 4 pixels applied. The colorbar represents (smoothed) photon counts. For visualization purposes, different cuts were use for the middle and right image. Most of the group emission is visible in the lower energy band (0.2 to 2.3 keV).

3.2 Image filtering

Each skytile is cleaned individually using `evtool` with `pattern=15` to select all event patterns and `flag=0xe00fff30` to remove bad pixels and CCD corners. Subsequently, soft proton flares are identified and mitigated through the following process: the `flaregti` task is used to generate light curves with 20 s time bins in the energy range of 5 to 10 keV. A 3σ threshold is determined; time intervals where count rates exceed this threshold are likely due to soft proton flares. The task `flaregti` is then rerun using this threshold to establish good-time-intervals (GTIs) excluding these flare periods, which are applied using `evtool` with the `gti="FLAREGTI"` parameter. All SPF-filtered and cleaned skytiles are combined into a single TM0 photon image using `evtool`. Hereafter, these combined images shall be referred to as “filtered”.

3.3 Exposure map and image creation

The `evtool` task, along with the `telid` parameter, is used to split the TM0 filtered photon images into individual filtered images for each TM. These images are then resized to the soft-band and the hard-band using `evtool` with the parameters `emin` and `emax`. For subsequent PIB and exposure corrections, both vignetted and flat (non-vignetted) exposure maps are generated for each TM in the soft band using the `expmap` task with the `withvignetting` parameter. Moreover, the `withdetmaps` parameter is specified to crop the images at the edge of the field of view for each TM. By keeping `withmergedmaps` at its default value of `YES`, merged all-telescope exposure maps are created. This means the exposure maps consider the 7 TMs as one TM with on-chip TM, assuming the combined effective area of the 7 on-chip TMs. The vignetted and flat exposure maps can be found in Appendix TODO.

3.4 PIB Correction

It is necessary to subtract the particle-induced background (PIB) from the combined filtered photon image. The following approach is based on extensive studies of the eROSITA filter wheel closed (FWC) data conducted by Dr. F. Pacaud, as utilized for example in Reiprich, Veronica, et al., 2021. The PIB is modeled for each TM using FWC data. Due to the minimal spatial variation of the PIB, this modeling utilizes the flat exposure map created in 3.3. Furthermore, given the negligible spectral variation, the counts H_{obs} in the hard band, where PIB counts dominate, is used to estimate the PIB contribution in the soft bands by multiplication with the ratio R of the number of FWC counts in the soft band S_{FWC} to the hard band H_{FWC}. The PIB-background map for each TM is then generated by applying this factor to the flat exposure map, normalized to 1 by dividing by the sum of all pixel values (norm. flat exposure map). Hence, the PIB map of a given TM is given by

$$\text{PIB map}_{\text{TM}} = H_{\text{obs}} R \cdot \left(\text{norm. flat exposure map}\right).$$

Soft-band, PIB-corrected image are obtained by subtracting the PIB map of each TM from the respective soft-band, filtered photon image. The complete image for TM0 is obtain by co-adding all PIB corrected images. To better visualize the PIB-correction, individual background maps are also co-added to form a complete PIB map, which can be found in Appendix A.1. Table TODO contains the obtained H_{obs} and R values.

3.5 Absorption Correction

As discussed in Section 2.3, X-ray absorption by the ISM must be considered. To correct for this absorption, the methodology outlined in Willingale et al., 2013 is followed. Additionally, scripts for the absorption correction were provided by Angie Veronica (as utilized in Veronica, 2020). At higher energies ($\gtrsim 0.2\,\text{keV}$), as is relevant for this analysis, absorption from metals play a significant role. Assuming solar metallicity, the hydrogen column density (N_{H}) can used to trace the absorbing material. A cutout of the HI4PI all-sky survey (HI4PI Collaboration et al., 2016) is reprojected onto relevant sky tiles to create a neutral atomic hydrogen map (N_{HI}-map). Additionally, a molecular hydrogen map (N_{H_2}-map) is constructed by dividing the full sky image into 52×52 pixel cells, querying N_{H_2} values from the Swift homepage[3], and distributing these values across each cell. The total N_{Htot}-map, constructed by $N_{\text{Htot}} = N_{\text{H}} + 2N_{\text{H}_2}$, is shown in Appendix TODO, with N_{H} ranging from $N_{\text{Htot, min}} = 2.91 \times 10^{20}\,\text{cm}^{-2}$ to $N_{\text{Htot, max}} = 1.61 \times 10^{21}\,\text{cm}^{-2}$. Next, for a each individual N_{H}-value in the N_{Htot}-map, the expected soft band count rates for TM1 and TM5 – which serve as proxies for TM8 and TM9, respectively, due to their similar area and response files – are simulated for the model

$$\text{apec}_{\text{LHB}} + \text{ph}_{\text{abs.}} \cdot (\text{apec}_{\text{MWH}} + \text{pow})$$

[3] https://www.swift.ac.uk/analysis/nhtot/index.php (Last accessed: 25.07.2024)

using XSPEC[4] with the `fakeit` command and their respective area (ARF) and response files (RMF). Here, apec_{LHB} represents unabsorbed Local Hot Bubble emission, $\text{ph}_{\text{abs.}}$ the absorption along the line of sight, apec_{MWH} the absorbed Milky Way Halo emission, and pow the absorbed emission from unresolved point sources (e.g., AGNs). A correction factor A_{corr} is determined for each value of N_{H} by dividing the simulated count rate for the N_{Htot}-map median $\left(\overline{N_{\text{Htot}}}\right)$ by the simulated count rate of the N_{H} of interest, hence

$$A_{\text{corr}}(N_{\text{H}}) = \frac{\text{simulated count rate}\left(\overline{N_{\text{Htot}}}\right)}{\text{simulated count rate}\left(N_{\text{H}}\right)}.$$

Finally, each N_{H} in the N_{Htot}-map is replaced by the corresponding correction factor A_{corr} to create an absorption correction map. Absorption correction maps are created for both TM1 and TM5.

3.6 Exposure Correction

The counts image of any given X-ray observation inherently depends on a detector's effective area and the telescope's pointing motion throughout the observation. To obtain meaningful flux units (e.g. $\text{cts} \cdot \text{arcsecond}^{-2}\text{s}^{-1}$), these effects must be considered. This is achieved by dividing the count image by the vignetted exposure map created in Section 3.3, thereby rescaling all segments of the count image to the same relative exposure (Davis, 2001). However, an exposure map must be created separately for TM8 and TM9 due to three reasons: first, TM9 uses a narrow energy band, which lowers its expected count rate; second, this narrower energy band necessitates a different absorption correction map; third, TM8 and TM9 have very distinct area response files because of their different filter configurations. Thus, both exposure maps cannot simply be combined but must be corrected for these effects. The procedure outlined in Reiprich, Veronica, et al., 2021 will be followed. First, the vignetted exposure map of TM8 and TM9 are divided by their respective absorption correction maps to obtain an absorption-corrected exposure map ($\text{exmap}_{\text{TM8, corr}}$, $\text{exmap}_{\text{TM9, corr}}$). Second, the ratio of PIB-corrected count rates of TM8 and TM9 is used to define a correction factor

$$E_{\text{corr}} = \frac{\text{PIB corr. count rate(TM9)}}{\text{PIB corr. count rate(TM9)}}$$

The total absorption-corrected exposure map for TM0 is then given by

$$\text{exmap}_{\text{TM0, corr}} = \text{exmap}_{\text{TM8, corr}} + E_{\text{corr}} \cdot \text{exmap}_{\text{TM9, corr}}$$

A correction factor of $E = 0.4628$ is obtained. Dividing the filtered and PIB-corrected soft-band TM0 image by its absorption-corrected exposure map results in the final filtered, PIB-corrected, absorption-corrected, and exposure-corrected soft-band image. Henceforth, this will be referred to as the "corrected" soft-band image. Figure 3.2 compares the filtered, full energy-band count rate image (the filtered full band counts image divided by its respective exposure map) with the corrected soft-band image, both smoothed using a Gaussian kernel of 12 pixels. It is evident that group emission

[4] https://heasarc.gsfc.nasa.gov/xanadu/xspec/ (Last accessed: 25.07.2024)

can be much better distinguished from the background in the corrected soft-band image. Additionally, the previous count drop on the right side of the image, as seen in Figure **??**, has been addressed through the exposure correction.

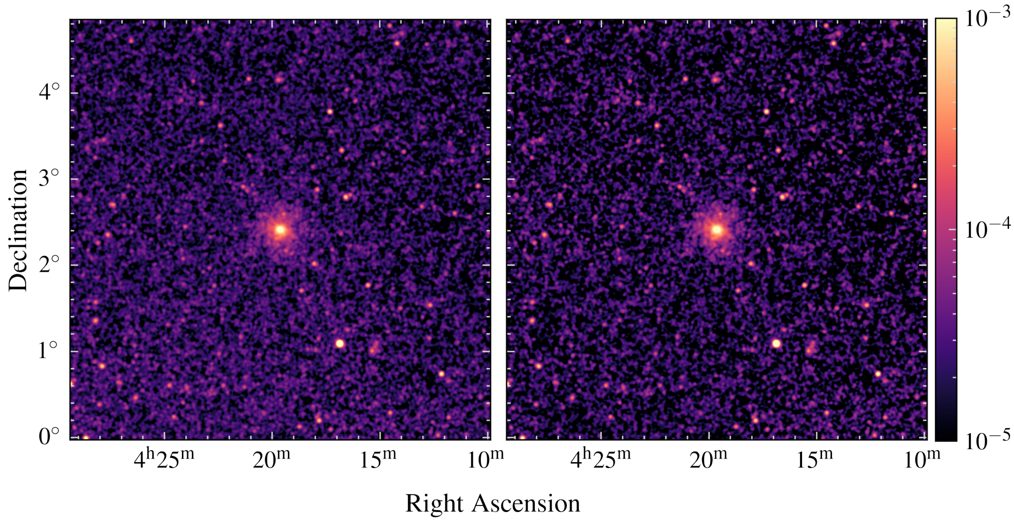

Figure 3.2: Comparison between the filtered, full energy-band count rate image (left) and the final corrected count rate image (right), both smoothed using a Gaussian kernel of 12 pixels. The corrected image clearly shows improved differentiation of group emission from the background in comparison to the filtered, full band image.

3.7 Wavelet filtering and Point Source Removal

It is necessary to remove the emission from point-like sources (e.g. AGNs) to prevent interference with the group emission under study. This is achieved using the wavelet filtering pipeline as described in Pacaud et al., 2006. Wavelet transformation decomposes an image $I(x, y)$ into coefficients $(w_1, \ldots, w_n, c_n)$

$$I(x, y) = c_n(x, y) + \sum_{j=1}^{n} w_j(x, y).$$

Here, $c_n(x, y)$ is the smoothed image, and $w_j(x, y)$ essentially represents the contribution of a wavelet function at a scale j and position (x, y) to the total image. By retaining only the coefficients that satisfy

$$|w_j(x, y)| > k\sigma_j,$$

where σ_j is the standard deviation at scale j and k is a clipping factor, and then applying the inverse wavelet transformation, an image is obtained that includes only significant scales, i.e. those not due to noise (Starck, J.-L. and Pierre, M., 1998). The resultant image is referred to as a wavelet-filtered image. In the pipeline being used, the absorption-corrected exposure map, $\mathrm{exmap}_{\mathrm{TM0,\,corr}}$, and the raw photon image are used to account for previous data reduction and to statistically handle the Poisson noise. After wavelet filtering, a source catalogue is obtained running `SExtractor` (Bertin and Arnouts, 1996). This is enabled by the significant noise reduction and smoothed background achieved by the wavelet filtering. The extended X-ray emission near NGC1550 is manually removed from the catalog, and a cheese-mask is created from the catalog and applied to $\mathrm{exmap}_{\mathrm{TM0,\,corr}}$. Emission around unrelated, but projectionally nearby, clusters and groups is also manually added to the cheese-mask. Rerunning wavelet filtering with the cheese-masked map reduces ringing artifacts, which typically occur near bright sources with steep flux gradients. Figure 3.3 compares the wavelet filtering before and after application of the cheese-mask to the exposure map.

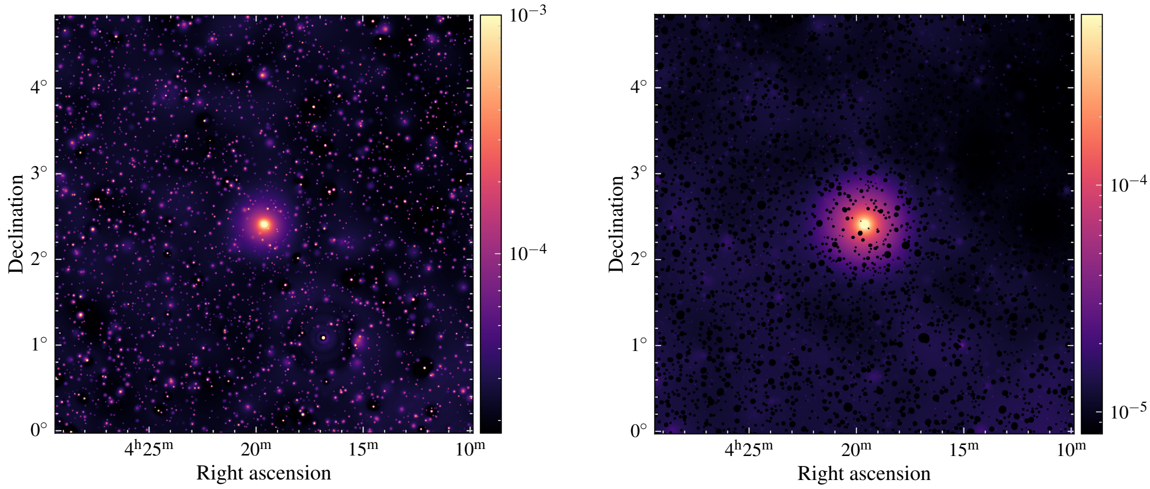

(a) Before applying the cheese-mask

(b) After applying the cheese-mask

Figure 3.3: Corrected wavelet filtered image before (left) and after (right) applying the cheesemask created with `SExtractor`. The left image is normalized such that the ringing artifacts are more prominent. The cheese-masked image has significantly reduced ringing artifact and group emission is well visible.

CHAPTER 4

Data Analysis

4.1 Image Inspection and galaxy distribution

A contour plot of the corrected and cheese-masked wavelet-filtered image is shown in Figure 4.2 to visualize emission beyond R_{500} more clearly. Furthermore, galaxy distribution using data from NASA/IPAC Extragalactic Database (NED) is extracted within a 1° radius of the galaxy group NGC 1550 and overlayed. There are 26 galaxies with similar redshifts $0.01 \le z \le 0.015$ including the galaxy NGC 1550 itself. From Figure 4.2 it is clear that the group appears spherically symmetrical and relaxed, with a distinct emission cutoff visible at R_{500}. Beyond this radius, emission becomes difficult to distinguish from the background, which is fairly complex due to the Orion-Eridanus superbubble (cf. Section 2.3). There is a noticeable gradient in the background emission, with a lower background to the north compared to the south. The galaxy distribution is loosely clustered to the northeast, but no clear correlation with the X-ray contours is observed. Usually, this helps indicate whether excess emission along a certain direction is significant.

To highlight emission structures within R_{500}, Figure 4.1 presents a contour plot of the corrected image smoothed with a Gaussian kernel of 8 pixels. Within this radius, some deviations from perfect azimuthal symmetry are noticeable. A slight east-west elongation within approximately $390''$ (inner circle in the figure) can indeed be inferred as mentioned in Section 2.1.4. Beyond $390''$, features are harder to distinguish: the emission in the north, south and east appear slightly more irregular. Emission in the west, falls more uniformly and there seems to be slight emission dip between $390''$ and $810''$ (outer circle in the figure) compared to the other sectors.

4.2 Full Azimuthal Surface Brightness Profile

To more accurately identify or exclude potential deviations from spherical symmetry, surface brightness (SB) analysis will be performed. First, the emission center is estimated by constructing a $2'$ aperture around the apparent center (right ascension 64.9066° and a declination 2.4151°). This aperture size is chosen to capture a statistically significant number of photons without leaving the group center. The flux-weighted average coordinates of the fully corrected image within this aperture

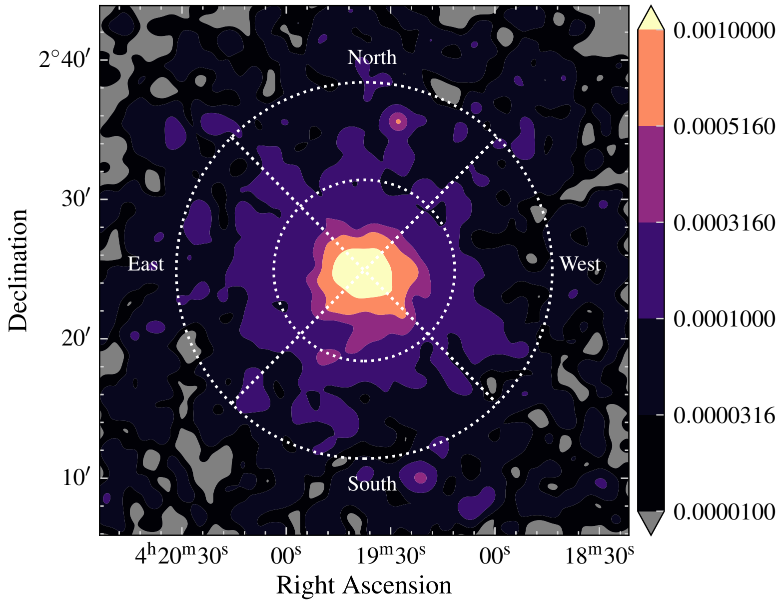

Figure 4.1: Contour plot of the corrected 8 pixel Gaussian smoothed image. The color bar indicates counts per second. Some deviations from azimuthal symmetry are observed within the outer circle ($\sim 810''$). The inner circle denotes a radius of $\sim 390''$. Within this region, an east-west elongation of the core is noticeable. The four wedges labeled north, south, east, and west correspond to the angular (but not radial) ranges used to extract surface brightness.

yields a right ascension of 64.909° and a declination of 2.414° and shall be referred to as the SB-center. Concentric anulli of $1'$ width are constructed from the SB-center up to to an angular distance of $80' \sim 1.5R_{200}$. The counts C within each annulus are determined using the `funcnts` task from the `funtools` software, with a Poisson error of $\sqrt{C}$. The surface brightness S for each annulus is calculated by

$$S = \frac{C_{\text{filt}} - C_{\text{PIB}}}{C_{\text{expmap}} \cdot A},$$

where C denotes the counts in the filtered photon image, total PIB map, and exposure map, respectively and A is the anullus area. Errors are calculated using Gaussian error propagation. Furthermore, background estimation is performed using 10 circular regions with a $30'$ radius, each centered at a distance of $100'$ from the SB-center (Figure TODO). The average background surface brightness is evaluated for all circles combined and separately for the northern (Circles 1-5) and southern region (Circles 6-10) to account for the possibly significant background gradient. Table 4.1 lists the average background for all 3 cases. As is clear from the table, the total background level is consistent with the other two within a 1σ-Intervall. Therefore, unless otherwise specified, the total background value derived from all circles will be used for the subsequent analysis and interpretation. A beta Model (cf.

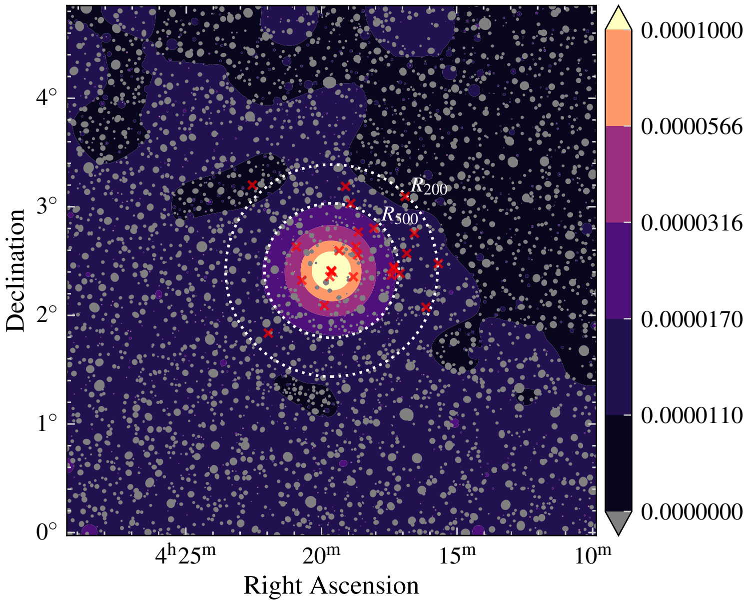

Figure 4.2: Contour plot of the corrected, cheese-masked, wavelet-filtered image with overlaid galaxy distribution (red crosses) within a 1° radius of NGC 1550. The color bar represents counts per second. The plot shows a distinct emission boundary at R_{500}, with emission beyond this radius becoming difficult to distinguish from the background. The galaxy distribution is clustered to the northeast, though no clear correlation with the X-ray contours is observed.

Region	Background / cts s^{-1} $arcsec^{-2}$
North	$(1.03 \pm 0.10) \times 10^{-7}$
South	$(1.27 \pm 0.04) \times 10^{-7}$
Total	$(1.15 \pm 0.14) \times 10^{-7}$

Table 4.1: Surface brightness and associated errors for the different background regions.

Section 2.1.3) is employed to characterize the surface brightness profile, given by

$$S_X(r) = S_X(0)\left(1 + \left(\frac{r}{r_c}\right)^2\right)^{-3\beta+0.5} + d$$

where d represents the background emission. The center of each annulus is taken to be r and the corresponding surface brightness values are utilized. The optimized parameters and χ^2/d.o.f (Chi squared per degrees of freedom) are listed in Table 4.2. Figure 4.3 illustrates the surface brightness as a function of radial distance from the center, including both the fitted beta model and the observationally estimated background level.

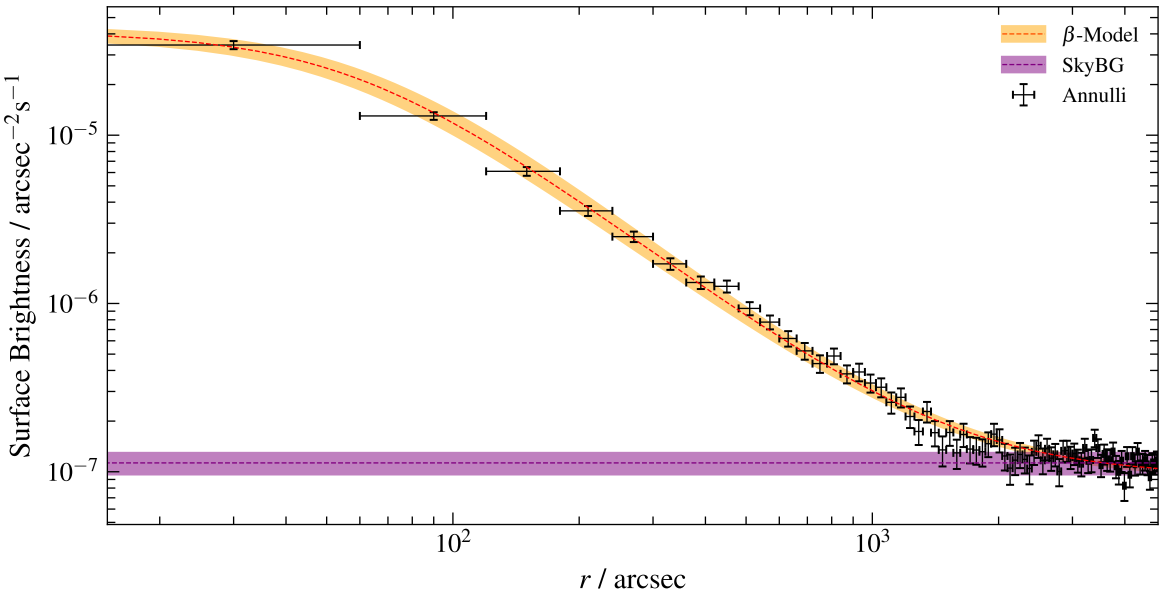

Figure 4.3: Surface Brightness within each annulus (black crosses) as a function of distance from the determined SB-center including error bars. The dashed orange line represents the best beta model fit, while the purple line indicates the observationally determined background. The shaded regions correspond to their respective 1σ intervals.

Parameter	S_0 / cts s^{-1} arcsec^{-2}	β	r_c / $''$	d / cts s^{-1} arcsec^{-2}
	$(4.1 \pm 0.4) \times 10^{-5}$	0.478 ± 0.008	60 ± 5	$(9.3 \pm 0.4) \times 10^{-8}$
χ^2/d. o. f		0.96		

Table 4.2: Fit parameters, their errors, and the reduced chi-squared value for the full azimuthal surface brightness profile.

The beta model fit for the surface brightness profile, shown in Figure 4.3, yields $\beta = 0.478 \pm 0.008$

and core radius $r_c = (60 \pm 5)'' \sim (15 \pm 2)$ kpc with χ^2/d.o.f. = 0.96. This result is consistent with previous studies: Kawaharada, Makishima, Takahashi, et al., 2003 report $\beta = 0.47$ and $r_c \sim (16 \pm 1)$ kpc using ASCA data; Kawaharada, Makishima, Kitaguchi, et al., 2009 use a two-beta model to find $\beta = 0.50 \pm 0.05$ and $r_c \sim (20 \pm 3)$ kpc for the outer component from XMM-Newton data; Sun et al., 2003 also derive $\beta \sim 0.48$ and a slightly higher $r_c \sim 26$ kpc for the outer component using Chandra data; Reiprich and Böhringer, 2002, although, report a somewhat higher $\beta = 0.554^{+0.049}_{-0.037}$ using ROSAT. The surface brightness profile also highlights that the group emission decreases to the background level at approximately R_{500}, as observed in Section 4.1. The observationally estimated total background in Table 4.1, however, is approximately 24% higher than the background obtained by the beta-model fit (cf. Table 4.2) at 1.5σ. Although this discrepancy is not too alarming, it does indicate challenges associated with the complex background, indicating that they could have been chosen more carefully.

A two-beta model fit was not successful. This can be attributed to the angular resolution of the $1'$ width anulli, limiting the ability to resolve the inner core emission. Perfoming a beta-model fit with finer annuli was attempted, but this did not significantly improve the description of the surface brightness profile within the core and resulted in poor error estimation in the outskirts due to low count rates. Indeed, Kawaharada, Makishima, Kitaguchi, et al., 2009 find an inner core component of $r \sim 3$ kpc corresponding to $\sim 12''$ which is comparable to the eROSITA angular resolution $\sim 15''$ (Predehl et al., 2021).

4.2.1 Beta Model and Residual Image

Using the parameters from Table 4.2, a beta model image (Fig. 4.4) and a residual image (Fig. 4.5) are created. The beta model image is generated by distributing the one-dimensional beta model across the image. This involves computing the distance from the surface brightness center to each coordinate (x, y) in the image and then scalling the output of the beta model by the eROSITA pixel area of 16arcsec^2. The residual image (res. img) was obtained by subtracting the scaled beta model from the corrected soft-band image (corr. img). Hence,

$$\text{res. img}(x, y) = \text{corr. img}(x, y) - S\left(\sqrt{x^2 + y^2}\right) \cdot \text{pix. area}.$$

The residual image indicates that the beta model underestimates the emission around the core. This can be attributed to the absence of a second beta component, as a single beta model often inadequately describes the inner core emission, which is often higher-than-expected. Sun et al., 2003 report, however, that even a two-beta fit is not sufficient to describe the surface brightness within the central 1 kpc. Disregarding the excess emission within the core, no significant substructure or features can be noticed from the residual image.

4.3 Sectorial Surface Brightness Analysis

Thus far, the surface brightness analysis has encompassed the entire azimuthal extent of the group. By analyzing surface brightness within specific sectors and comparing them to the full azimuthal

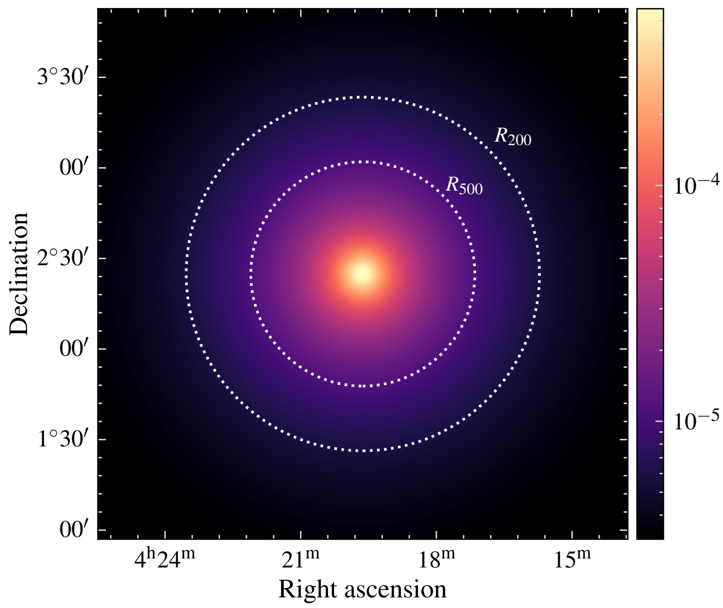

Figure 4.4: Beta model image of NGC1550 utilizing the parameters in 4.2. The colorbar represents counts per second.

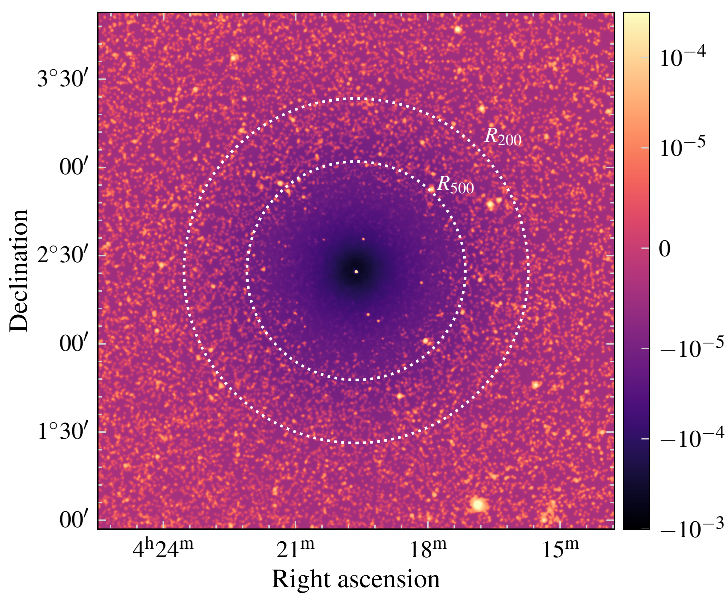

Figure 4.5: Residual image of NGC1550 derived by subtracting beta model image from the corrected soft-band image. The colorbar represents counts per second and the image has been smoothed with a Gaussian-kernel of 5 pixels. The residual image indicate that the beta model slightly overestimates the emission around the core, due to the inadequacy of a single beta model in capturing the core's emission.

profile, elongation in certain directions can be revealed. Various authors have reported an east-west elongation at the center of NGC1550 (Sun et al., 2003, Kolokythas et al., 2020), making it particularly interesting to determine whether this elongation extends into the outer regions of the group. To investigate this, four sectorial regions (north, south, east, and west) are divided into annuli, as shown in Figure 4.1. The center, width and extension of the annuli remain as described in Section 4.1, and surface brightness calculations and beta model fitting follow the same methodology.

Each region is initially fitted individually. Thereafter, the north and south sectors are fitted together, as are the east and west sectors. Figure 4.6(a) illustrates the comparison between the east and west profiles and Figure 4.6(b) compares the north and south profiles. The top graph shows the surface brightness profiles, including the observationally determined sky background and the corresponding beta model. The lower two graphs display the relative surface brightness differences of each region (SB_{sec}) compared to the full azimuthal surface brightness profile (SB_{an}). The error bars represent the error of the relative difference computed by Gaussian error propagation. The fit parameters for each beta model are listed in Table 4.3.

The fits are of lower quality (χ^2/d.o.f. $\lesssim 0.8$), suggesting possible overfitting or, more likely, an overestimation of the errors as attempts using wider $2'$ annuli resulted in significantly improved χ^2/d.o.f. $\gtrsim 0.95$ for the west, north, and combined east-west profiles, and a modest improvement for the remaining sectors. These fit parameters and χ^2/d.o.f. values are detailed in Appendix TODO. However, since the full azimuthal analysis was only performed with the smaller annuli and the resulting fit parameters are similar across both cases, the smaller annuli will be utilized for the following comparison.

In all sectors, no notable deviation from the full azimuthal profile is observed beyond $100'$. When inspecting the western region, the emission dip observed in the western region between approximately $810''$ and $390''$–as noted in section 4.1–is noticeable in relation to the full azimuthal surface brightness plot. However, these deviations are not quantitatively significant and may be attributed to statistical fluctuations. For the northern and southern sectors, a deviation is noted at the first data point. This discrepancy is likely due to a suboptimal choice of the annuli center and is probably not physically significant. The combined east-west and north-south emissions are compared in Figure 4.7 with the beta model parameters also listed in 4.3. Here, too, no significant deviation from the full azimuthal profile is observed beyond the first data point, indicating that the east-west elongation seen within the $390''$ does not extend towards the outskirts of the group. It can be noticed, however, that the

Parameter	S_0 / cts s^{-1} arcsec^{-2}	β	r_c / $''$	d / cts s^{-1} arcsec^{-2}	χ^2/d. o. f
East+West	$(2.88 \pm 0.27) \times 10^{-5}$	$(5.08 \pm 0.12) \times 10^{-1}$	$(8.60 \pm 0.80) \times 10^{1}$	$(1.02 \pm 0.05) \times 10^{-7}$	0.83
North+South	$(6.20 \pm 0.71) \times 10^{-5}$	$(4.58 \pm 0.07) \times 10^{-1}$	$(4.01 \pm 0.43) \times 10^{1}$	$(8.45 \pm 0.46) \times 10^{-8}$	0.71
West	$(3.42 \pm 0.42) \times 10^{-5}$	$(5.20 \pm 0.16) \times 10^{-1}$	$(8.11 \pm 0.98) \times 10^{1}$	$(9.63 \pm 0.60) \times 10^{-8}$	0.77
East	$(3.18 \pm 0.43) \times 10^{-5}$	$(4.87 \pm 0.15) \times 10^{-1}$	$(7.22 \pm 0.97) \times 10^{1}$	$(1.02 \pm 0.07) \times 10^{-7}$	0.82
North	$(2.23 \pm 0.35) \times 10^{-5}$	$(4.49 \pm 0.14) \times 10^{-1}$	$(6.6 \pm 1.1) \times 10^{1}$	$(7.89 \pm 0.78) \times 10^{-8}$	0.78
South	$(1.10 \pm 0.20) \times 10^{-4}$	$(4.69 \pm 0.10) \times 10^{-1}$	$(3.32 \pm 0.53) \times 10^{1}$	$(8.69 \pm 0.64) \times 10^{-8}$	0.86

Table 4.3: Fit parameters, their errors, and the reduced chi-squared value for the beta model fit of the north, south, east and west sectors and the combined north-south and east-west sectors.

β parameter and the core radius r_c are not always consistent when comparing the sectors against

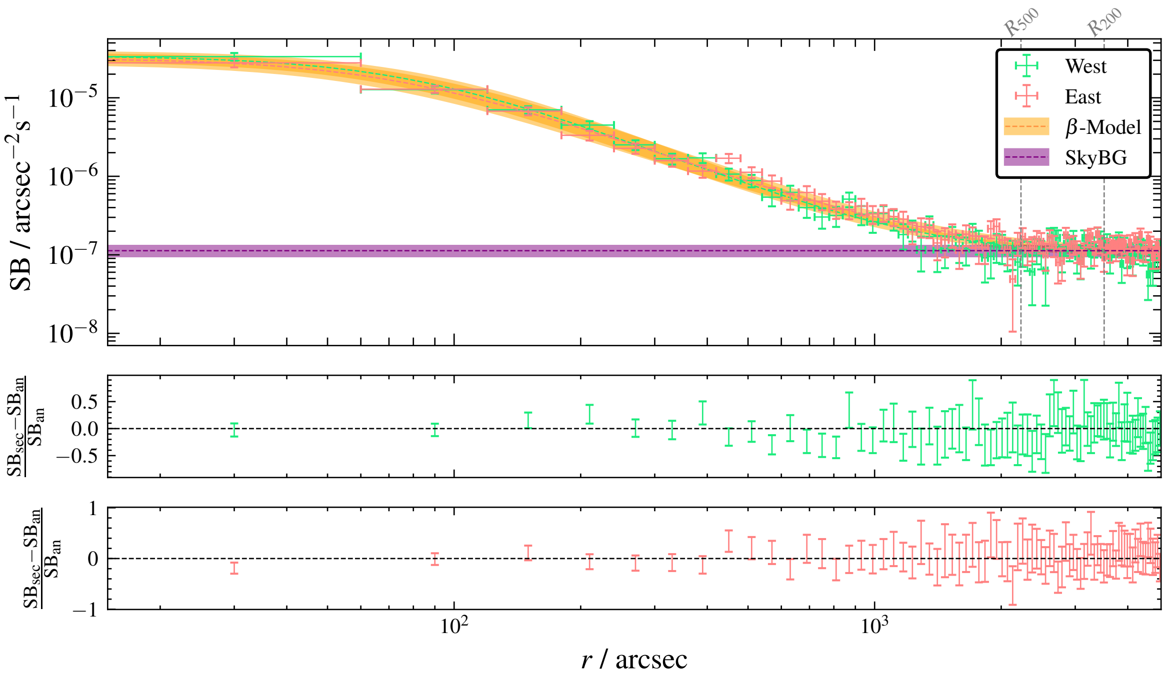

(a) Beta model fits for the West and East regions.

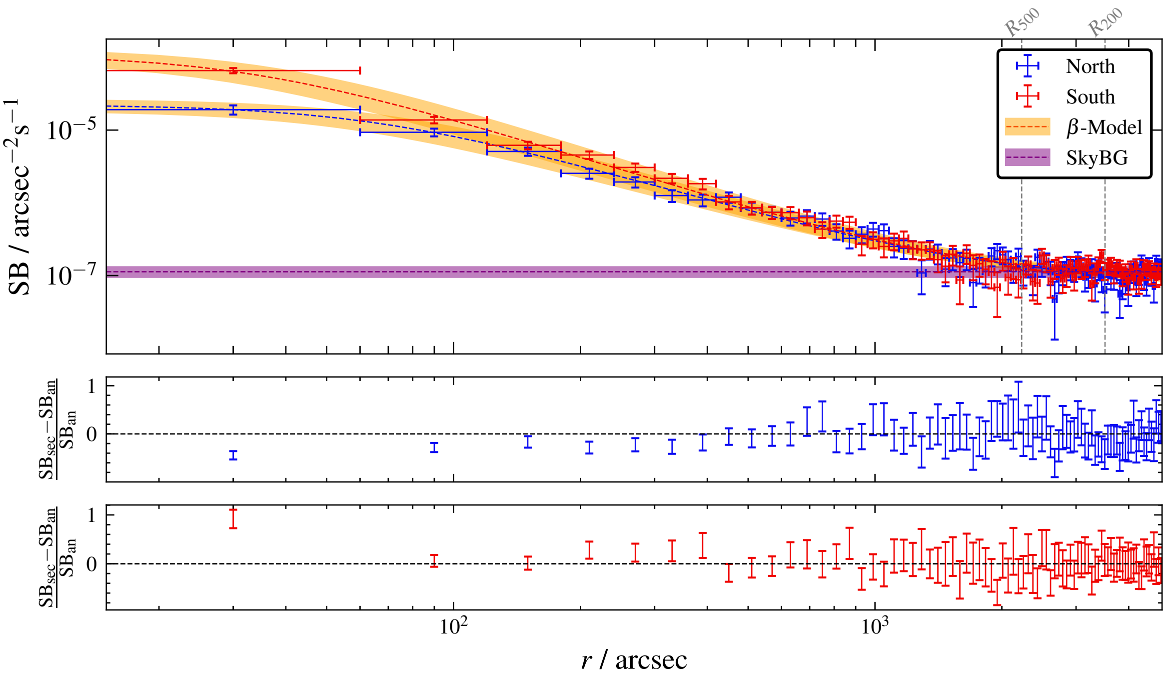

(b) Beta model fits for the North and South regions.

Figure 4.6: Beta model fits for the West-East and North-South regions. The surface brightness profiles are shown in the top graph, including the observationally determined sky background and the respective beta model. The lower two graphs display the relative surface brightness differences between each region (SB_{sec}) and the full azimuthal surface brightness profile (SB_{an}) with error bars from Gaussian error propagation. No significant deviation from the full azimuthal profile is observed beyond 100″.

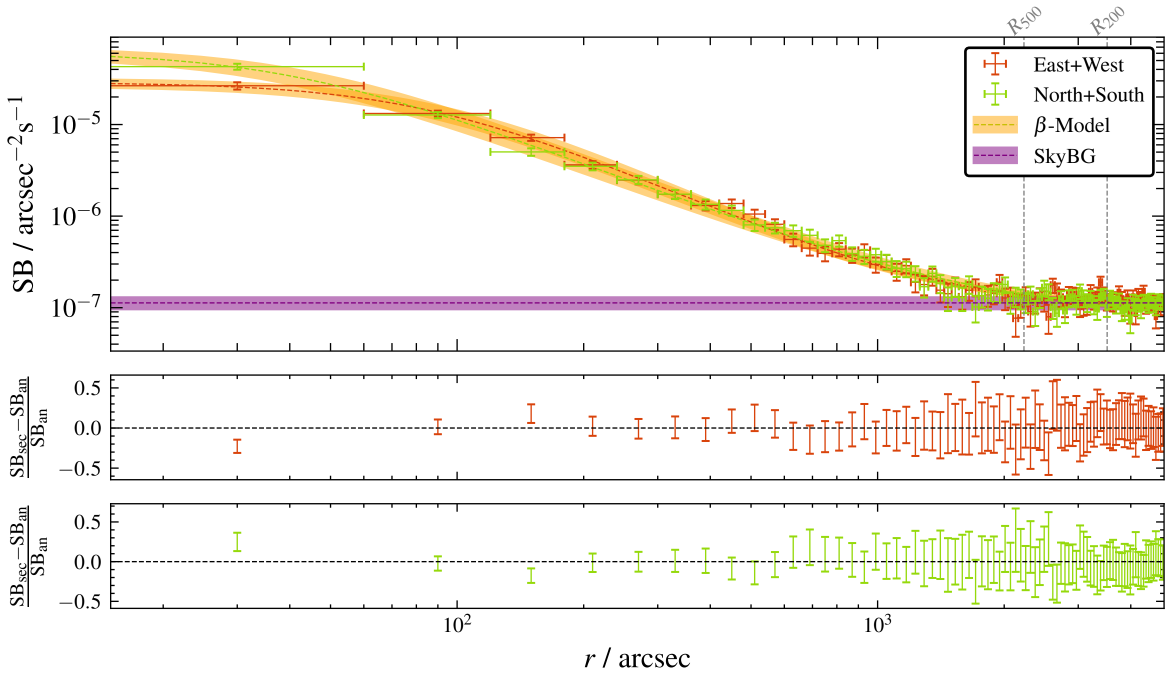

Figure 4.7: Beta model fits for the combined east-west and north-south regions. The surface brightness profile is show in the top graph and the lower two graphs display the relative surface brightness differences between each region ($\mathrm{SB}_{\mathrm{sec}}$) and the full azimuthal surface brightness profile ($\mathrm{SB}_{\mathrm{an}}$). Error bars are derived from Gaussian error propagation. Excluding the first data point, both combined surface brightness profiles show no significant deviation from the full azimuthal profile and are entirely consistent with another, indicating no significant east-west elongation in the outskirts of the galaxy group.

each other and with the full azimuthal profile. Notably, the core radius r_c for the combined east-west region is more than twice as large as that for the combined north-south region, and the β value is approximately 10% larger, with discrepancies at $> 5\sigma$ and $> 3\sigma$, respectively. In fact, most of the β-values and core radii are inconsistent within a 1σ interval when comparing the sectors. This discrepancy may result from a poor SB-center choice, biasing the surface brightness towards the south. For instance, the southern sector's normalization factor S_0 shows a relative difference of almost 80% compared to the north sector, with a 4.32σ deviation. Consequently, the estimated SB-center at 64.909° and 2.414° is likely too far north, leading to an overestimation of southern emission in the initial data points. This issue is exacerbated by the wide $1'$ annuli, meaning that excess emission of the first data point might be significantly affecting the fits.

Regarding the background, the fitted background level for the east, west, and combined east-west regions is consistent with the total background level. However, for the northern and southern regions, the fitted background level underestimates the observationally determined background level by 31% and 46%, at 1.9σ and 0.98σ, respectively. This discrepancy might indicate poorly chosen background regions or could be due to the inherently complex background.

CHAPTER 5

Conclusion

5.1 Results and discussion

In the surface brightness analysis in Chapter 4, a contour plot of the corrected, cheesemasked wavelet filtered image in the soft-band with an overlaid galaxy distribution was provided. From this, it was established that the galaxy group NGC1550 appears relaxed and spherically symmetrical. However, within 810′′, some indications of asymmetry were visually identified using a contour plot of the corrected image. Emission was found to drop off to background levels at R_{500}, with a somewhat complex background noted, which can be attributed to the Orion-Eridanus superbubble. No obvious correlation between the X-ray contours and the galaxy distribution could be ascertained.

To more accurately characterize the morphology of NGC1550 in the X-ray, a surface brightness analysis was performed. A β-model was employed to characterize the full azimuthal profile, as shown in Figure 4.3. The model fitting yielded a β-value of 0.478 ± 0.008 and a core radius of approximately $r_c = 60'' \sim (15 \pm 2)$ kpc, with a reduced chi-squared value of 0.96, indicating a good fit. This result was consistent with the findings of various authors, showing that the eROSITA view of NGC1550 aligns with previous findings. However, the analysis also highlighted a slight discrepancy between the observationally estimated background and the fitted background level, suggesting complexities in background estimation that could affect the surface brightness measurements.

The residual image indicated that the beta model underestimates the core emission, as is common, but no other features were detected. Attempts to use a two beta model were unsuccessful, likely due to the large width of the annuli and the small inner core component, which, from previous studies (Kawaharada, Makishima, Kitaguchi, et al., 2009), is of order of eROSITA's angular resolution. A successful two-β model might have been possible by, for example, fixing the inner core radii or convolving the model with the eROSITA point spread function, but this was attempted within the scope of this thesis.

Moreover, the sectorial surface brightness analysis across the northern, southern, eastern, and western sectors, as well as the combined northern-southern and eastern-western sectors, revealed no significant deviations from azimuthal symmetry. Individual beta fits had slightly lower quality ($\chi^2 \lesssim 0.8$), likely due to the low count numbers per annulus. Although regional surface brightness profiles did not deviate significantly from the azimuthal profile, their fit parameters, particularly the β

parameters and core radii across sectors, varied significantly. It was speculated that this could be due to a poor choice of the SB-center, creating a significant discrepancy between the north and south emission for the first data point at $\sim 60''$.

A potential solution would be a two-dimensional fit of the full azimuthal beta model, allowing free SB-center fitting and better estimation, or simply a more careful selection of the SB-center. Ignoring this issue, however, deviations in fit parameters might be taken as an indication, that galaxy groups do not exhibit perfect azimuthal symmetry, with infalling matter causing inevitable deviations. However, due to the complex background obscuring diffuse group emission in the outskirts and the aforementioned fitting issues, it is challenging to definitively conclude if the findings of this thesis support this view.

5.2 Outlook

Given that only eRASS:1 data was utilized, several features that were qualitatively observed, such as a slight emission dip in the western sector between $\sim 390''$ and $\sim 810''$, could not be quantitatively verified. With additional data, such as from eRASS:3, these features could be more accurately interpreted and their significance better assessed. The increased data would also allow for finer annuli in the surface brightness analysis due to the higher count rates in each annulus bin, facilitating better feature identification and potentially simplifying a two-beta model fit.

Furthermore, future work could leverage eROSITA to perform detailed spectroscopy of the outskirts of NGC1550. X-ray spectroscopic measurements can provide insights into the enrichment of the intracluster medium (ICM) and the historical processes of galaxy groups or clusters Liu et al., 2020. Understanding the distinctions in enrichment processes between galaxy groups and clusters remains an ongoing challenge. eROSITA's wide field of view presents a unique opportunity to study these processes in greater detail, enhancing our knowledge of the chemical composition and evolutionary history of NGC 1550 and similar systems. (TODO: more precise?)

Appendix

APPENDIX A

Appendix

A.1 PIB Map

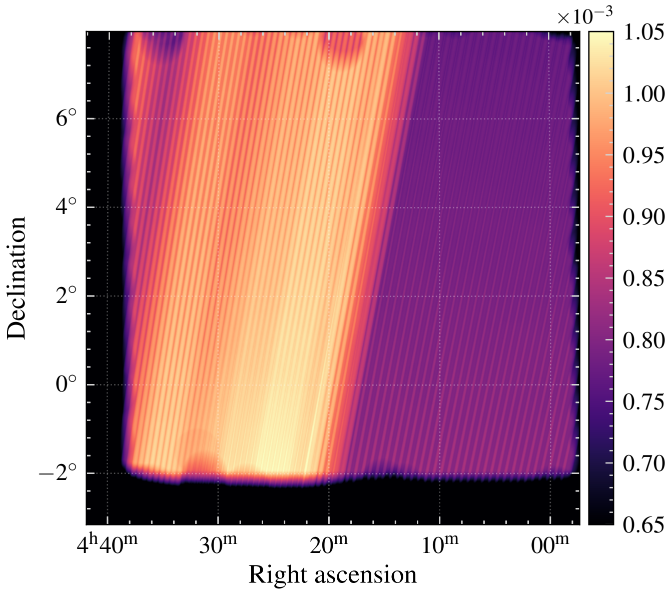

Figure A.1: PIB map created by co-adding individual background maps for each telescope module (TM).

Bibliography

Bertin, E. and S. Arnouts (1996), *SExtractor: Software for source extraction.*, **117** 393 (cit. on p. 12).

Böhringer, H. et al. (2000), *The Northern ROSAT All-Sky (NORAS) Galaxy Cluster Survey. I. X-Ray Properties of Clusters Detected as Extended X-Ray Sources*, **129** 435, arXiv: `astro-ph/0003219 [astro-ph]` (cit. on pp. 1, 3).

Brandt, W. and G. Hasinger (2005), *Deep Extragalactic X-ray Surveys*, Annual Review of Astronomy and Astrophysics **43** 827, First published online as a Review in Advance on June 14, 2005 (cit. on p. 4).

Bulbul, E. et al. (2020), *Characterization of the Particle-induced Background of XMM-Newton EPIC-pn: Short- and Long-term Variability*, The Astrophysical Journal **891** 13, URL: `https://dx.doi.org/10.3847/1538-4357/ab698a` (cit. on p. 5).

Cavaliere, A. and R. Fusco-Femiano (1976), *X-rays from hot plasma in clusters of galaxies.*, **49** 137 (cit. on p. 3).

Cavaliere, A. G., H. Gurksy, and W. H. Tucker (1971), *Extragalactic X-ray Sources and Associations of Galaxies*, Nature **231** 437, ISSN: 1476-4687, URL: `https://doi.org/10.1038/231437a0` (cit. on p. 2).

Collaboration, T. A. et al. (2022), *The Astropy Project: Sustaining and Growing a Community-oriented Open-source Project and the Latest Major Release (v5.0) of the Core Package**, The Astrophysical Journal **935** 167, ISSN: 1538-4357, URL: `http://dx.doi.org/10.3847/1538-4357/ac7c74` (cit. on p. 7).

Davis, J. E. (2001), *The Formal Underpinnings of the Response Functions Used in X-Ray Spectral Analysis*, The Astrophysical Journal **548** 1010, © 2001. All rights reserved. Printed in U.S.A. (cit. on p. 10).

Fukugita, M., C. J. Hogan, and P. J. E. Peebles (1998), *The Cosmic Baryon Budget*, **503** 518, arXiv: `astro-ph/9712020 [astro-ph]` (cit. on p. 1).

Galeazzi, M., A. Gupta, K. Covey, and E. Ursino (2006), *XMM-Newton observations of the diffuse X-ray background*, Department of Physics, University of Miami (cit. on p. 4).

HI4PI Collaboration et al. (2016), *HI4PI: A full-sky H I survey based on EBHIS and GASS*, Astronomy & Astrophysics **594** A116, URL: `https://ui.adsabs.harvard.edu/abs/2016A&A...594A.116H` (cit. on p. 9).

Hunter, J. D. (2007), *Matplotlib: A 2D graphics environment*, Computing in Science & Engineering **9** 90 (cit. on p. 7).

Jones, L. et al. (2003), *The nature and space density of fossil groups of galaxies*, MNRAS **343** (cit. on p. 3).

Kawaharada, M., K. Makishima, T. Kitaguchi, et al. (2009), *A GALAXY MERGER SCENARIO FOR THE NGC 1550 GALAXY FROM METAL DISTRIBUTIONS IN THE X-RAY EMITTING PLASMA*, The Astrophysical Journal **691** 971, URL: https://dx.doi.org/10.1088/0004-637X/691/2/971 (cit. on pp. 1, 3, 17, 22).

Kawaharada, M., K. Makishima, I. Takahashi, et al. (2003), *A New Candidate for the Dark Group of Galaxies, RX J0419+0225*, **55** 573 (cit. on pp. 1, 3, 17).

King, I. (1962), *The structure of star clusters. I. an empirical density law*, **67** 471 (cit. on p. 3).

Kolokythas, K. et al. (2020), *Evidence of AGN feedback and sloshing in the X-ray luminous NGC 1550 galaxy group*, Monthly Notices of the Royal Astronomical Society **496** 1471, ISSN: 1365-2966, URL: http://dx.doi.org/10.1093/mnras/staa1506 (cit. on pp. 4, 19).

Krause, M., R. Diehl, H. Böhringer, M. Freyberg, and D. Lubos (2014), *Feedback by massive stars and the emergence of superbubbles: II. X-ray properties*, Astronomy & Astrophysics **566** A94, ISSN: 1432-0746, URL: http://dx.doi.org/10.1051/0004-6361/201423871 (cit. on pp. 4, 5).

Kravtsov, A. V. and S. Borgani (2012), *Formation of Galaxy Clusters*, Annual Review of Astronomy and Astrophysics **50** 353, ISSN: 0066-4146, eprint: https://www.annualreviews.org/doi/pdf/10.1146/annurev-astro-081811-125502, URL: https://www.annualreviews.org/doi/10.1146/annurev-astro-081811-125502 (cit. on pp. 1, 2).

Liu, A. et al. (2020), *The chemical evolution of galaxy clusters: Dissecting the iron mass budget of the intracluster medium*, Astronomy & Astrophysics **637** A58, Published online 14 May 2020, URL: https://doi.org/10.1051/0004-6361/202037506 (cit. on p. 23).

Pacaud, F. et al. (2006), *The XMM Large-Scale Structure survey: the X-ray pipeline and survey selection function*, Monthly Notices of the Royal Astronomical Society **372** 578, ISSN: 0035-8711, eprint: https://academic.oup.com/mnras/article-pdf/372/2/578/2937517/mnras0372-0578.pdf, URL: https://doi.org/10.1111/j.1365-2966.2006.10881.x (cit. on p. 11).

Predehl, P. et al. (2021), *First science highlights from SRG/eROSITA: The eROSITA X-ray telescope on SRG*, A&A **647** A1 (cit. on pp. 4, 5, 17).

Reiprich, T. H., A. Veronica, et al. (2021), *The Abell 3391/95 galaxy cluster system: A 15 Mpc intergalactic medium emission filament, a warm gas bridge, infalling matter clumps, and (re-) accelerated plasma discovered by combining SRG/eROSITA data with ASKAP/EMU and DECam data*, AandA **647** A2, URL: https://doi.org/10.1051/0004-6361/202039590 (cit. on pp. 9, 10).

Reiprich, T. H. and H. Böhringer (2002), *The Mass Function of an X-Ray Flux-limited Sample of Galaxy Clusters*, The Astrophysical Journal **567** 716, URL: https://dx.doi.org/10.1086/338753 (cit. on pp. 3, 7, 17).

Reiprich, T. H. and F. Pacaud (2019), *Multiwavelength Observations of Galaxy Clusters*, (cit. on p. 3).

Sato, K. et al. (2010), *Metallicity of the Fossil Group NGC 1550 Observed with Suzaku*, Publ. Astron. Soc. Jap. **62** 1445, arXiv: 1009.4173 [astro-ph.CO] (cit. on pp. 1, 4).

Schneider, P. (2006), *Extragalactic Astronomy and Cosmology: An Introduction*, Second Edition, Springer-Verlag Berlin Heidelberg 2006, ISBN: 978-3-642-54082-0 (cit. on pp. 1, 2).

Starck, J.-L. and Pierre, M. (1998), *Structure detection in low intensity X-ray images*, Astron. Astrophys. Suppl. Ser. **128** 397, URL: https://doi.org/10.1051/aas:1998150 (cit. on p. 12).

Sun, M. et al. (2003), *Chandra Observations of the NGC 1550 Galaxy Group: Implication for the Temperature and Entropy Profiles of 1 keV Galaxy Groups*, The Astrophysical Journal **598** 250, URL: https://dx.doi.org/10.1086/378887 (cit. on pp. 1, 3, 4, 17, 19).

Veronica, A. (2020), *X-ray Studies of the Interacting Galaxy Cluster System Abell 3391 and Abell 3395 Using eROSITA and XMM-Newton*, Masterthesis in Astrophysics, MA thesis: Argelander-Institut für Astronomie, Mathematisch-Naturwissenschaftliche Fakultät der Rheinischen Friedrich-Wilhelms-Universität Bonn (cit. on p. 9).

Willingale, R., R. L. C. Starling, A. P. Beardmore, N. R. Tanvir, and P. T. O'Brien (2013), *Calibration of X-ray absorption in our Galaxy*, **431** 394, arXiv: 1303.0843 [astro-ph.HE] (cit. on pp. 6, 9).

List of Figures

List of Tables